

Fluid Flow and Defect Formation in the Three-Dimensional Dendritic Structure of Nickel-Based Single Crystals

J. MADISON, J.E. SPOWART, D.J. ROWENHORST, L.K. AAGESEN, K. THORNTON, and T.M. POLLOCK

Fluid flow within the dendritic structure at the solid–liquid interface in nickel-based superalloys has been studied in two directionally solidified alloy systems. Millimeter-scale, three-dimensional (3D) datasets of dendritic structure have been collected by serial sectioning, and the reconstructed mushy zones have been used as domains for fluid-flow modeling. Flow permeability and the influence of dendritic structure on flow patterns have been investigated. Permeability analyses indicate that the cross flow normal to the withdrawal direction limits the development of flow instabilities. Local Rayleigh numbers calculated using the permeabilities extracted from the 3D dataset are higher than predicted by conventional empirical calculations in the regions of the mushy zone that are prone to the onset of convective instabilities. The ability to measure dendrite surface area in 3D volumes permit improved prediction of permeability as well.

DOI: 10.1007/s11661-011-0823-8

© The Minerals, Metals & Materials Society and ASM International 2011

I. INTRODUCTION

DIRECTIONAL solidification provides control of the orientation and growth of columnar grain and single-crystal materials.^[1,2] This advancement in processing has yielded a significant improvement in the high-temperature creep and fatigue properties of nickel-based superalloys.^[1–4] Unfortunately, depending on alloy and process conditions, directional solidification may result in the formation of grain defects such as misoriented, high-angle grain boundaries and/or freckle chains.^[4–7] The frequency of such defects has been shown to be related directly to slower cooling rates that characteristically produce coarser dendritic structures and larger interdendritic porosity.^[7] Advanced alloys with higher levels of refractory alloying elements and large, more geometrically complex cast components are even more prone to defect formation. Thus, accurate solidification models that can predict the conditions under which these defects form as well as provide input

to alloy and component design can clearly provide substantial benefits.^[5,6,8–16]

During directional solidification, an inversion in the solute density gradient can lead to localized fluid flow, resulting in flow channels compositionally rich in interdendritic solute.^[5–11] These channels or “chimneys” are the precursor event to the breakdown of single-crystal solidification, as the local transport of molten alloy upward through the melt can fragment, erode, and transport solidified material to various locations in the melt. These transported fragments migrate primarily toward the walls of the casting and may form large misoriented grains or chains of fragments, termed “freckle chains” shown in Figure 1.

These grain defects develop when a critical solute-induced density gradient allows the buoyant forces in the melt to overcome the frictional drag forces of the environment; therefore, the Rayleigh number (Ra_h) is often used as a quantitative predictor for the conditions associated with defect formation.^[8,11,13,14]

$$Ra_h = \frac{(\Delta\rho/\rho_o)g\bar{K}h}{\alpha\nu} \quad [1]$$

The density gradient in the liquid is denoted by the term $(\Delta\rho/\rho_o)$, g is the acceleration because of gravity, α is thermal diffusivity, ν is kinematic viscosity, and \bar{K} is the average permeability. Among the aforementioned examples, permeability is the only factor derived typically by means other than direct assessment from the chemistry and thermodynamics of the system. Permeability can vary by orders of magnitude within the mushy zone,^[17–21] so the details of the dendritic structure can influence the Rayleigh number strongly. Permeability has typically been defined empirically with consideration of flow through porous media.^[17,20–28] More recently, computational analyses of permeability

J. MADISON, Senior Member of Technical Staff, is with the Computational Materials Science & Engineering Department, Sandia National Laboratories, Albuquerque, NM 87185. Contact e-mail: jdmadis@sandia.gov J.E. SPOWART, Senior Materials Research Engineer, is with the Air Force Research Laboratory/RXBC, Wright Patterson AFB, OH 45433. D.J. ROWENHORST, Metallurgist, is with the Naval Research Laboratory, Washington, DC 20375. L.K. AAGESEN, Post-Doctoral Associate, and K. THORNTON, Associate Professor, are with the Department of Materials Science & Engineering, University of Michigan, Ann Arbor, MI 48109. T.M. POLLOCK, Professor, is with the Department of Materials, University of California at Santa Barbara, Santa Barbara, CA 93106.

Manuscript submitted January 31, 2011.

Article published online July 22, 2011

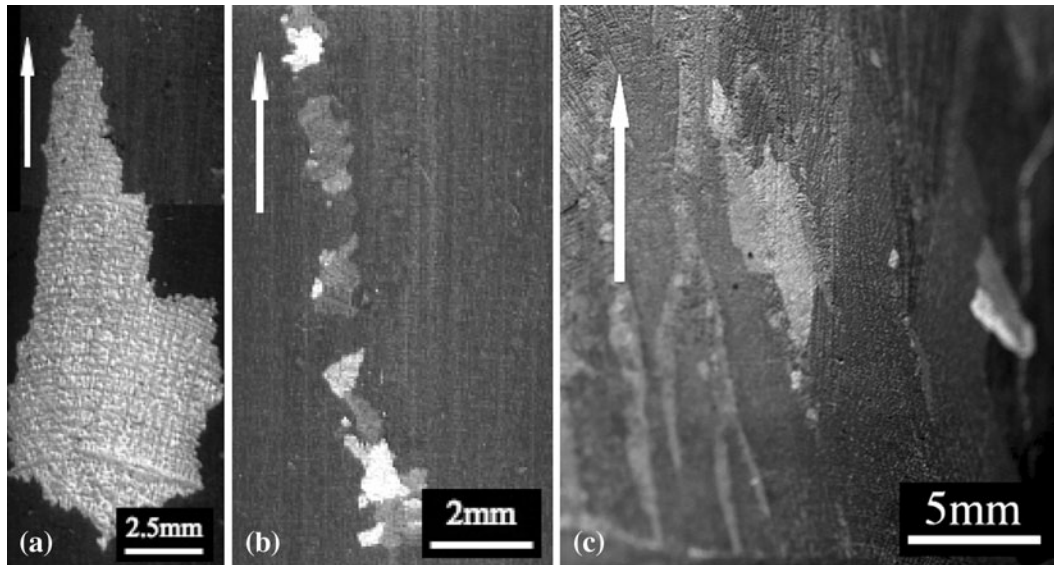


Fig. 1—(a) Single misoriented grain and (b) freckle chain in directionally solidified castings (adapted in part from Ref. 14, as well as (c) freckles observed in Ni-Al-W casting in current study. In all cases, the primary growth direction is indicated by an arrow.

have been performed with more accurate representations of the dendritic structure, albeit with relatively small volumes considered.^[18,19,29–31] Other difficulties associated with assessment of the Rayleigh number in superalloy solidification include (1) accurate prediction of solute density gradients in the mushy zone,^[32,33] (2) selection of an optimal length scale that encompasses the scale of convective potential accurately,^[12,13] and (3) accurate knowledge of thermal diffusivity and kinematic viscosity in multicomponent alloy systems.

The current investigation uses experimentally derived, 3D dendritic networks removed from the solidification front for simulation of isothermal, noncompressible fluid flow for direct permeability assessment. The relatively large volume of the reconstructed dendritic structure, with micrometer-scale resolution, permits the analysis of flow properties across multiple primary and secondary dendrites and from dendrite tips to deep within the mushy zone. Two different alloys with substantially different dendritic structure have been studied. The relationship of dendritic structure to interfacial surface area (ISA), flow tortuosity (T_{avg}), and resulting permeability (K) are examined, and the implications for the development of convective instabilities are addressed.

II. EXPERIMENTAL METHOD AND COMPUTATIONAL APPROACH

Using an ALD Vacuum Technologies furnace, ingots ranging from 4.5 to 5.5 kg were directionally solidified at the University of Michigan by the conventional Bridgman process to produce single crystals. ALD Vacuum Technologies, Inc. is located in Hanau, Germany and is a wholly owned subsidiary of Advanced Metallurgical Group. Two alloys were investigated: the second-generation commercial superalloy René N4, with a nominal composition of Ni-4.2Al-0.05C-7.5Co-9.8Cr-0.15Hf-

1.5Mo-0.5Nb-4.8Ta-3.5Ti-6.0W (wt pct) and a model ternary, Ni-6.5Al-9.5W (wt pct). Withdrawal rates of 2.5 mm/min and 3.3 mm/min were used for René N4 [$T_{liquidus} = 1618$ K (1345 °C), $T_{solidus} = 1573$ K (1300 °C)] and the Ni-Al-W ternary alloy [$T_{liquidus} = 1729$ K (1456 °C), $T_{solidus} = 1706$ K (1433 °C)], respectively. During withdrawal, controlled fractures of the mold wall were initiated, allowing the evacuation of molten liquid and producing isolated dendritic structures accessible for investigation. Material containing the transition from fully solidified regions to dendrite tips was extracted from the castings, serial sectioned with the prototype RoboMet.3DTM* system^[34] located within the

*RoboMET.3DTM is a trademark of UES Inc. which is headquartered in Dayton, OH.

Materials and Manufacturing Directorate of the Air Force Research Laboratory (AFRL/RX), and imaged parallel to the primary growth direction. Reconstructions of the solidification front in both materials are shown in Figure 2. After image segmentation and reconstruction, both 3D datasets were converted into tetrahedral meshed domains. This mesh was then subdivided into domains that spanned different volume fractions of the solid and were subsequently used as input structures in full Navier-Stokes finite-element, fluid-flow models in two orthogonal flow directions: vertical (*i.e.*, in the primary solidification direction) and cross (*i.e.*, in the secondary dendrite arm growth direction). Additional details of the casting and decanting process,^[35] serial sectioning and reconstruction,^[36] and fluid-flow simulations^[37] have been reported previously for René N4. In this investigation, a substantially different Ni-Al-W ternary alloy has been investigated, and more detailed analyses of the interfacial surface area and fluid flow in subdomains of both mushy zones are presented. The implications of fluid-flow

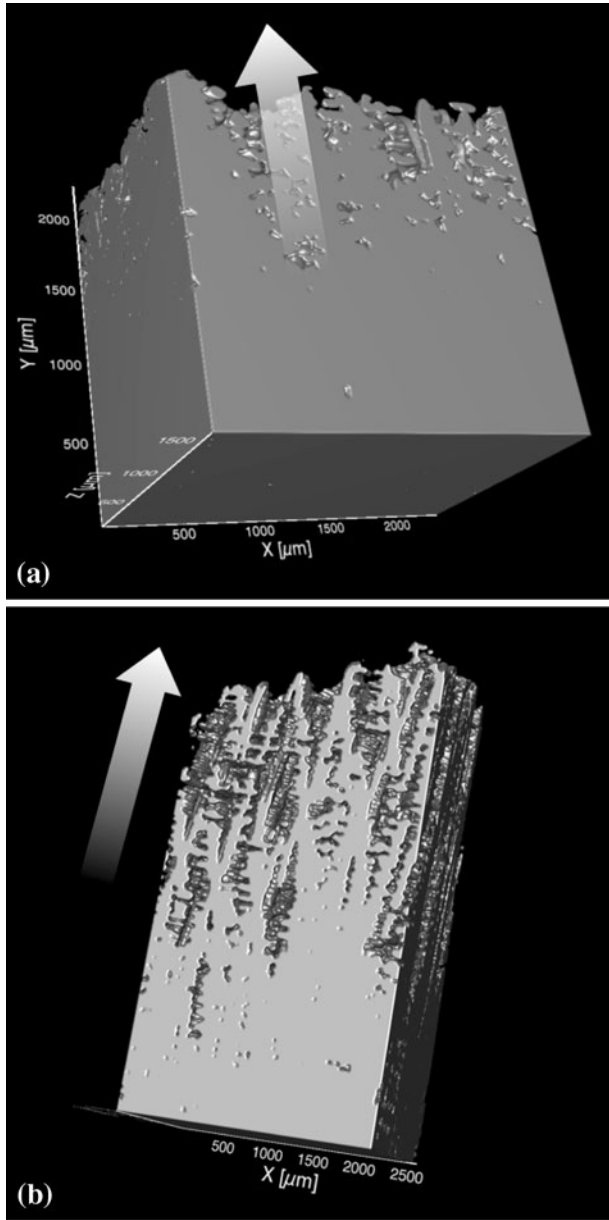


Fig. 2—Reconstructed datasets of midsolidification mushy zones in (a) René N4 (2.3 × 2.3 × 1.5 mm) and (b) Ni-Al-W ternary (2.5 × 5.0 × 1.6 mm).

behavior within these experimental domains for the development of convective instabilities are also considered for the first time.

III. RESULTS

A. Permeability Analysis

The dependence of flow behavior on fraction liquid was examined over the range of $0.10f_L - 0.90f_L$ in both the René N4 and the Ni-Al-W datasets. In René N4, six vertical-flow and four cross-flow cells were constructed for analysis. In the Ni-Al-W system, seven vertical-flow and seven cross-flow cells were used. Figures 3 and 4 illustrate the velocity fields in representative vertical and

cross-flow cases in both René N4 and Ni-Al-W datasets, respectively. The characteristics of individual flow-cell dimensions and related volume fraction solid are presented in Table I for René N4 and in Table II for Ni-Al-W. Darcy's law, Eq. [2], which describes the relation between Q , the volumetric flow rate; A , cross-sectional area; μ , the fluid viscosity; and L , the length associated with change in pressure across each flow cell, ΔP was used to calculate a local permeability (K) for each simulation cell. In this formulation, A corresponds to the cross-sectional area at the inlet of the cell.

$$Q = KA \frac{\Delta P}{\mu L} \quad [2]$$

Because permeability can be anisotropic based on the environment of flow, K_y for parallel flow and K_x for cross flow were independently calculated, and are listed as functions of inlet volume fraction for vertical flow cases and total volume fraction for cross flow instances. The calculated permeabilities and related values are summarized for each flow case in Table I for René N4 and Table II for Ni-Al-W, respectively.

Comparison of the permeabilities shown in Tables I and II with empirical permeability models reveals some interesting correlations. The directional Blake-Kozeny model (modified by Heinrich and Poirier for directionally solidified structures^[38]) takes the following form:

$$K_y = \begin{cases} 3.75 \times 10^{-4} f_L^2 d_1^2 & f_L \leq 0.65 \\ 2.05 \times 10^{-7} \left[\frac{f_L}{1-f_L} \right]^{10.739} d_1^2 & 0.65 \leq f_L \leq 0.75 \\ 0.074 \left[\ln(1-f_L) \right]^{-1} - 1.49 \\ + 2(1-f_L) - 0.5(1-f_L)^2 \Big] d_1^2 & 0.75 \leq f_L \leq 1.0 \end{cases} \quad [3]$$

$$K_x = K_{\text{cross}} \begin{cases} 1.09 \times 10^{-3} f_L^{3.32} d_1^2 & f_L \leq 0.65 \\ 4.04 \times 10^{-6} \left[\frac{f_L}{1-f_L} \right]^{6.7336} d_1^2 & 0.65 \leq f_L \leq 0.75 \\ \left(-6.49 \times 10^{-2} \right. \\ \left. + 5.43 \times 10^{-2} \left[\frac{f_L}{1-f_L} \right]^{0.25} \right) d_1^2 & 0.75 \leq f_L \leq 1.0 \end{cases} \quad [4]$$

In both Eq. [3] and [4], f_L refers to the volume fraction liquid and d_1 , and d_2 refer to the spacing of the primary and secondary dendrite arms, respectively. Although the dendritic structures investigated in this study are non-equiaxed, the isotropic Kozeny-Carmen model^[27,39] is also employed for comparison, Eq. [5], as it considers directly both the volume fraction solid f_S (where $f_L = 1 - f_S$) as well as the effects of interfacial surface area per unit volume (S_V) on permeability.

$$K_{KC} = \frac{f_L^3}{5S_V^2} = \frac{(1-f_S)^3}{5S_V^2} \quad [5]$$

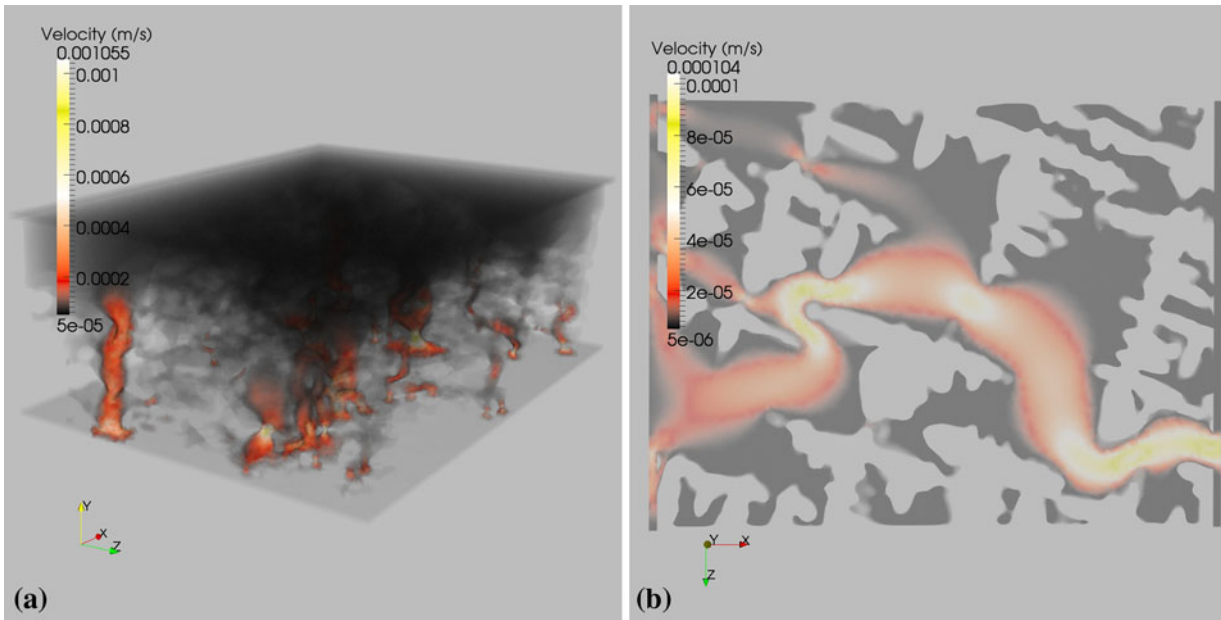


Fig. 3—Velocity magnitude fields for flow simulations in René N4 dataset; cases (a) N4-Y2 and (b) N4-X2, respectively.

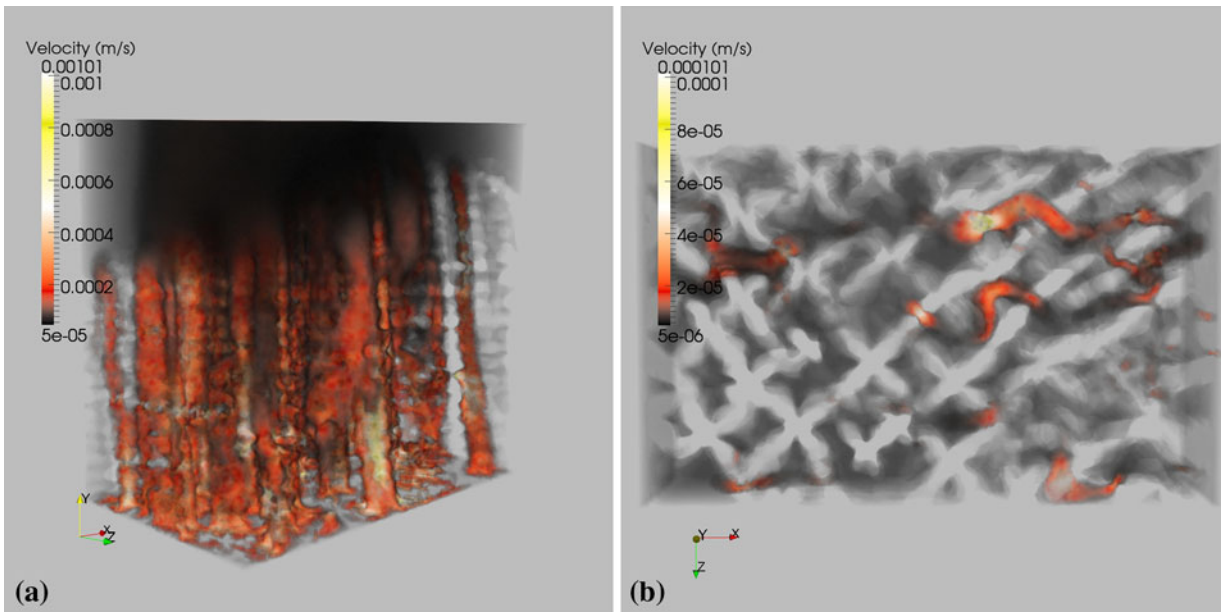


Fig. 4—Velocity magnitude fields for flow simulations in Ni-Al-W dataset; cases (a) NAW-Y3 and (b) NAW-X3, respectively.

Notably, Eq. [5] is similar in form to the basic Blake-Kozeny relation^[27,40]

$$K_{BK} = C_2 \frac{d_1^2 f_L^3}{(1 - f_L)^2} = C_2 \frac{d_1^2 (1 - f_S)^3}{f_S^2} \quad [6]$$

in which C_2 is a numerical constant optimized from experimental data. In an effort to employ consistent physical measures and provide a comparison with the permeabilities determined here (Tables I and II), a common approximation for average permeability used by various investigators^[11,13,14,41] will also be considered. This approximation assumes the following form:

$$\bar{K} = 6 \times 10^{-4} d_1^2 \frac{f_L^3}{(1 - f_L)^2} \quad [7]$$

where d_1 is again the primary dendrite arm spacing and 6×10^{-4} is a best fit coefficient derived from midrange experimental and low solid fraction theoretical data.^[42] A comparison of Eqs. [3–5] with calculated results from this study are shown in Figure 5 for René N4 and Figure 6 for the Ni-Al-W system.

The error bars in Figures 5 and 6 represent the local variation in solid fraction for each flow cell. Error bars for vertical flow permeabilities (K_y) are one sided as the

Table I. Summary of René N4 Flow Simulations and Calculated Permeabilities by Case

Case	Cell Volume (mm ³)	Inlet Volume Fraction Liquid	Velocity _{min} – max (mm/s)	Pressure Differential (Pa)	Length over Pressure Drop (×10 ⁻⁴ m)	Volumetric Flow Rate (×10 ⁻¹² m ³ /s)	Permeability (×10 ⁻¹¹ m ²)
Vertical Flow	N4-Y1	2.18 × 1.64 × 0.98	0.0532 – 1.06	7.7	2.4	19	0.11
	N4-Y2	2.18 × 1.65 × 0.84	0.0527 – 1.05	5.4	1.5	19	0.09
	N4-Y3	2.18 × 1.64 × 0.57	0.0537 – 1.07	5.2	1.5	170	1.3
	N4-Y4	2.18 × 1.65 × 0.48	0.0536 – 1.07	3.8	0.74	160	1.4
	N4-Y5	2.18 × 1.65 × 0.40	0.0538 – 1.08	5.5	0.55	240	1.8
	N4-Y6	2.18 × 1.65 × 0.35	0.0535 – 1.07	3.8	0.51	390	3.7
Case	Cell Volume (mm ³)	Volume Fraction Liquid	Velocity _{min} – max (mm/s)	Pressure Differential (Pa)	Length over Pressure Drop (× 10 ⁻⁴ m)	Volumetric Flow Rate (×10 ⁻¹² m ³ /s)	Permeability (×10 ⁻¹¹ m ²)
Cross Flow	N4-X1	2.16 × 1.62 × 0.03	0.00509 – 0.102	1.6	20	0.07	4.5
	N4-X2	2.16 × 1.62 × 0.02	0.00520 – 0.104	0.63	20	0.18	21
	N4-X3	2.16 × 1.62 × 0.01	0.00512 – 0.102	0.21	20	0.26	183
	N4-X4	2.16 × 1.62 × 0.01	0.00502 – 0.100	0.079	20	0.59	659

Table II. Summary of Ni-Al-W Ternary Flow Simulations and Calculated Permeabilities by Case

Case	Cell Volume (mm ³)	Inlet Volume Fraction Liquid	Velocity _{min} – max (mm/s)	Pressure Differential (Pa)	Length over Pressure Drop (×10 ⁻⁴ m)	Volumetric Flow Rate (×10 ⁻¹² m ³ /s)	Permeability (×10 ⁻¹¹ m ²)
Vertical Flow	NAW-Y1	2.59 × 1.63 × 3.60	0.051 – 1.03	3.01	3.00	53.2	5.20
	NAW-Y2	2.59 × 1.64 × 3.00	0.050 – 1.00	1.55	4.30	69.9	9.33
	NAW-Y3	2.59 × 1.64 × 2.50	0.051 – 1.01	1.82	4.00	200.5	13.7
	NAW-Y4	2.59 × 1.64 × 1.90	0.052 – 1.03	1.07	3.00	254.4	19.4
	NAW-Y5	2.59 × 1.64 × 1.20	0.051 – 1.02	3.57	1.40	436.3	36.5
	NAW-Y6a	2.59 × 1.64 × 0.96	0.051 – 1.02	1.12	0.49	691.3	52.9
	NAW-Y6b	1.29 × 1.64 × 0.74	0.051 – 1.02	1.47	0.50	334.8	41.7
Case	Cell Volume (μm ³)	Volume Fraction Liquid	Velocity Range (min – max) m/s	Pressure Differential (Pa)	Length over Pressure Drop (× 10 ⁻⁴ m)	Volumetric Flow Rate (×10 ⁻¹² m ³ /s)	Permeability (×10 ⁻¹¹ m ²)
Cross Flow	NAW-X1	1.34 × 1.63 × 0.47	0.0052 – 0.103	.922	10.7	0.106	0.43
	NAW-X2	2.60 × 1.63 × 0.67	0.0054 – 0.107	2.11	22.6	0.105	0.12
	NAW-X3	2.60 × 1.61 × 1.42	0.0051 – 0.101	.438	22.3	0.598	3.46
	NAW-X4	2.60 × 1.63 × 0.28	0.0054 – 0.108	.206	19.9	0.132	2.99
	NAW-X5	2.60 × 1.63 × 0.13	0.0050 – 0.100	.425	20.0	0.264	4.21
	NAW-X6	1.30 × 1.63 × 0.08	0.0052 – 0.104	.203	11.4	1.42	27.0
	NAW-X7	1.30 × 1.62 × 0.10	0.0053 – 0.107	.107	11.7	2.42	74.0

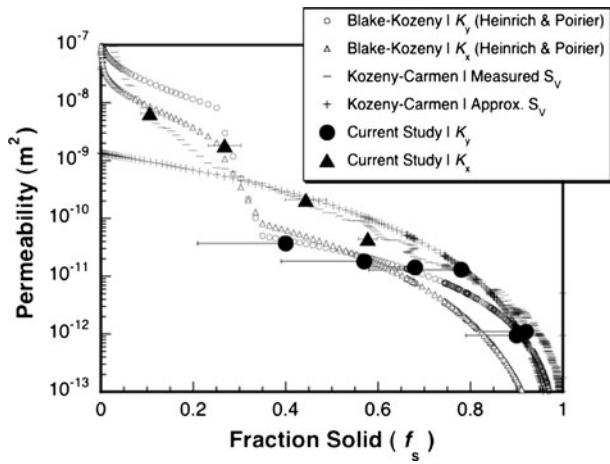


Fig. 5—Comparison of empirical Blake-Kozeny and Kozeny-Carmen permeability models with directly calculated permeability via 3D simulation in René N4.

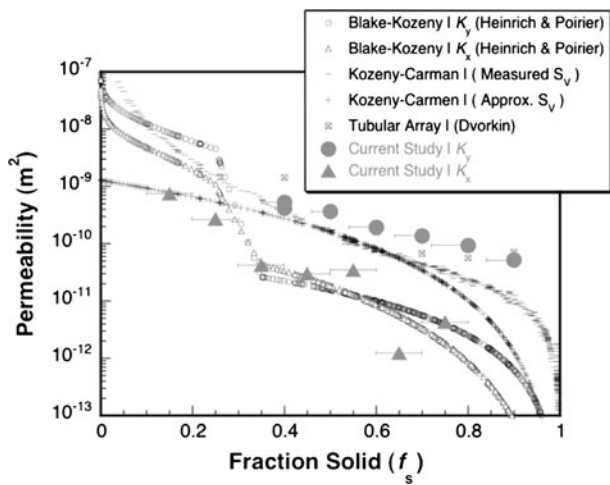


Fig. 6—Comparison of empirical Blake-Kozeny and Kozeny-Carmen permeability models with directly calculated permeability via 3D simulation in Ni-Al-W.

cross-sectional areas used in these permeability calculations occur at the inlets and yield the maximum fraction solid within each vertical flow cell.

For René N4, Heinrich-Poirier Blake-Kozeny models, $K_{BK(HP)}$, coincide well with directly assessed permeabilities across all vertical flow simulations with the exception of a minor deviation at $0.8 f_s$. $K_{BK(HP)}$ models also describe cross flow results well at high solid fraction but underestimate permeability in the range $0.4 < f_s < 0.6$. Conversely in this range, the Kozeny-Carmen model appears to accurately describe the cross flow permeability as determined by simulation. This would suggest that the interfacial surface area per unit volume has a significant influence on permeability near $0.50 f_s$ in cross flow for the experimentally observed morphology in René N4.

For Ni-Al-W, cross-flow permeabilities (K_x) show reasonable correlation with $K_{BK(HP)}$ prediction with departures at $0.15 f_s$, $0.55 f_s$, and $0.65 f_s$ by a factor of ± 5 .

The failure of the $K_{BK(HP)}$ criterion to predict permeability in these structures is likely due to large constrictions existing in cross flow resulting in the localization of relatively high velocity flow to select channels, Figure 4(b). Conversely, vertical flow permeabilities (K_y) are higher than all $K_{BK(HP)}$ by a factor of 15 to 20. Interestingly, in comparison to Kozeny-Carman predictions with measured S_v , K_y are higher by a maximum factor of five across all fractions solid with convergence between simulation results and K_{KC} prediction at $0.4 f_s$.

Due to the nearly linear channels apparent in vertical flow cases for the Ni-Al-W alloy, an empirical model describing permeability in an array of tubes was also considered^[43,44] in Eq. [8]

$$K_{Dvorkin} = \frac{N\pi}{A\tau 8} \left(\frac{2f_L}{S_V} \right)^4 \quad [8]$$

where N corresponds to the number of pipes within the array, A is the combined cross-sectional area available for flow through pipes, and τ is equal to $\sin^{-1}\alpha$, where α denotes the angle of inclination of the tubular array. Again, f_L and S_V are the volume fraction liquid and interfacial surface area per unit volume, respectively. To simplify the model, permeability was calculated assuming purely vertical flow ($\alpha = 1$, $\sin^{-1}\alpha = 90$ deg) and N was assumed to scale linearly with increases in volume fraction liquid. As shown in Figure 6, the Dvorkin tubular permeability ($K_{Dvorkin}$) compares reasonably well across all vertical flow simulation results with minor departures at 0.40 , 0.70 , and $0.80 f_s$. Interestingly, these fraction solids also coincide with emerging deviations with the K_{KC} predictions, suggesting the divergence from the global interfacial surface area approximation results in deviations from the $K_{Dvorkin}$ model in this range. Nonetheless, the Dvorkin model is a much better indication of the vertical flow behavior in the Ni-Al-W dataset than the Kozeny-Carmen or Blake-Kozeny models.

B. Dendrite Morphology Considerations

In both datasets, the relationship between ISA, tortuosity ($T_{avg.}$) and resulting permeability (K) was explored. The ISA normalized by the unit volume (S_v) and unit volume solid (S_{vS}) are shown for both datasets in Figure 7(a) and (b) as functions of the fraction solid. Note that S_{vS} is the interfacial surface area per unit volume solid and is related to S_v such that

$$S_{vS} = S_v / f_s \quad [9]$$

Here, S_v , $T_{avg.}$, and K for each determination of permeability are listed in Tables III and IV and are illustrated graphically in Figures 8 through 10.

It should be reiterated that vertical flow cells in Ni-Al-W simulations exhibit liquid domains of linear channels upward through the mushy zone, Figure 4(a), resulting in substantially higher permeabilities in vertical flow compared to the René N4 material. Consistent with this, the interfacial surface area per unit volume peaks much lower in the Ni-Al-W material as cross-sectional

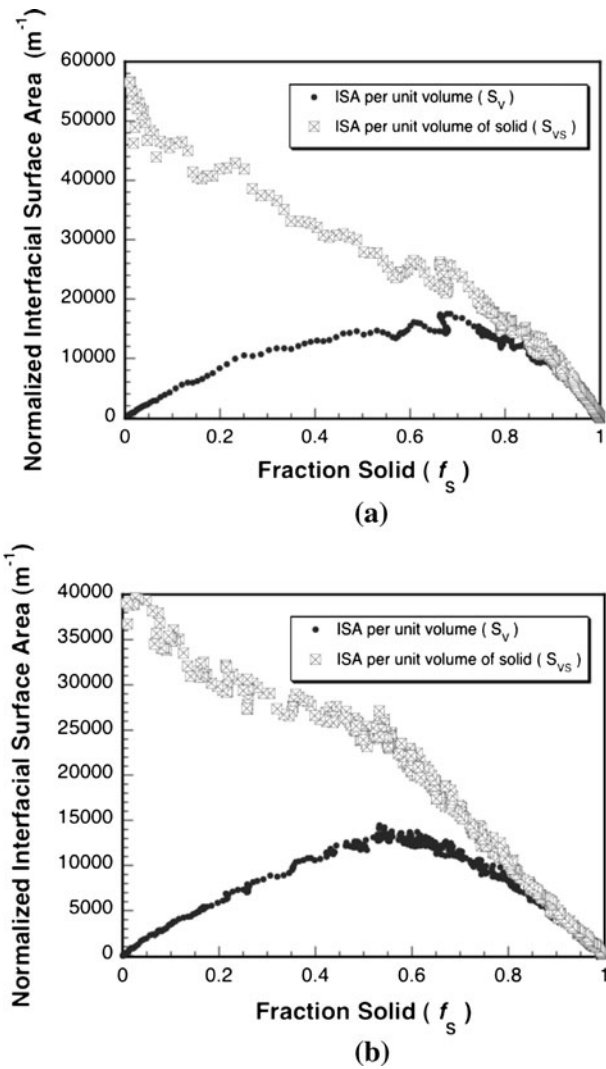


Fig. 7—Interfacial surface area per unit volume S_v , and per unit volume solid S_{vs} , in (a) René N4 and (b) Ni-Al-W datasets.

morphologies remain somewhat consistent throughout the height causing maximum ISA to coincide closely with 50 pct fraction solid (Figure 7).

Tortuosity ($T_{avg.}$), which is a measure of flow complexity, in this study is defined as the ratio of flow path length travelled through the simulation cell to the length of the pressure differential in each flow cell's permeability calculation, averaged over many uniformly distributed flow paths in the cell. Cross-flow tortuosity calculations contained between 120 and 650 streamlines per flow cell, whereas vertical flow tortuosity calculations ranged from 4000 to 150,000 streamlines per case because of the larger volumes considered. For linear flow paths, tortuosities close or equal to one would result. The more complex the flow path is, the higher the departure from a value of unity. In Figures 8 and 9, tortuosity is presented as a function of permeability across all vertical and cross-flow simulation cells. Larger volumes and the associated increase in streamlines per case contribute to the broader scatter observed in $T_{avg.}$ measures for vertical flow in comparison with those observed in cross flow. Furthermore, although there is much stronger variation in tortuosity within René N4 compared with Ni-Al-W across the mushy zone, decreases in $T_{avg.}$ coincide with increased permeability for vertical flow. The negligible change in $T_{avg.}$ for vertical flow within Ni-Al-W, which incidentally occurs at higher permeabilities than observed in René N4, results from near linear flow paths upward through the mushy zone. In cross flow, permeability (K_x), spans four orders of magnitude and while representing a range of 20 pct to 90 pct f_L there is nevertheless minimal variation in tortuosity. A limited variation of $T_{avg.}$ results from similar flow paths around the fourfold primary dendrites in both datasets regardless of the location in the mushy zone. This suggests that cross flow is influenced much more strongly by the fraction solid rather than by the interfacial surface area alone.

Table III. Flow Path Ratios, ISA Per Unit Volume & Permeability by Case for René N4 Simulations

Case		Inlet Volume Fraction Liquid	$T_{avg.}$ { \pm Var.}	Specific S_v ($\times 10^4$ m $^{-1}$)	Permeability ($\times 10^{-11}$ m 2)
Vertical Flow	N4-Y1	0.08	2.29 ± 0.83	58.1	0.11
	N4-Y2	0.10	2.56 ± 1.4	32.6	0.09
	N4-Y3	0.22	1.61 ± 0.33	57.0	1.3
	N4-Y4	0.32	1.57 ± 0.63	30.0	1.4
	N4-Y5	0.43	1.67 ± 0.63	19.4	1.8
	N4-Y6	0.60	1.51 ± 0.32	14.7	3.7
Case		Volume Fraction Liquid	$T_{avg.}$ { \pm Var.}	Specific S_v ($\times 10^4$ m $^{-1}$)	Permeability ($\times 10^{-11}$ m 2)
Cross Flow	N4-X1	0.42	1.26 ± 0.22	12.0	4.5
	N4-X2	0.56	1.39 ± 0.01	9.99	21
	N4-X3	0.73	1.21 ± 0.04	4.41	183
	N4-X4	0.89	1.13 ± 0.003	2.23	659

Table IV. Flow Path Ratios, ISA Per Unit Volume and Permeability by Case for Ni-Al-W Simulations

Case		Inlet Volume Fraction Liquid	$T_{avg.} \{ \pm Var \}$	Specific $S_V (\times 10^4 m^{-1})$	Permeability $(\times 10^{-11} m^2)$
Vertical Flow	NAW-Y1	0.10	1.30 ± 0.23	18.6	5.20
	NAW-Y2	0.20	1.18 ± 0.05	49.4	9.33
	NAW-Y3	0.30	1.16 ± 0.03	57.5	13.7
	NAW-Y4	0.40	1.25 ± 0.07	47.4	19.4
	NAW-Y5	0.50	1.19 ± 0.10	20.5	36.5
	NAW-Y6a	0.60	1.24 ± 0.17	7.37	52.9
	NAW-Y6b	0.60	1.27 ± 0.13	3.73	41.7
Case		Volume Fraction Liquid	$T_{avg.} \{ \pm Var. \}$	Specific $S_V (\times 10^4 m^{-1})$	Permeability $(\times 10^{-11} m^2)$
Cross Flow	NAW-X1	0.25	1.51 ± 0.11	26.3	0.43
	NAW-X2	0.35	1.19 ± 0.01	89.0	0.12
	NAW-X3	0.45	1.32 ± 0.03	66.2	3.46
	NAW-X4	0.55	1.24 ± 0.01	41.8	2.99
	NAW-X5	0.65	1.10 ± 0.01	16.7	4.21
	NAW-X6	0.75	1.24 ± 0.02	4.41	27.0
	NAW-X7	0.85	1.07 ± 0.01	3.55	74.0

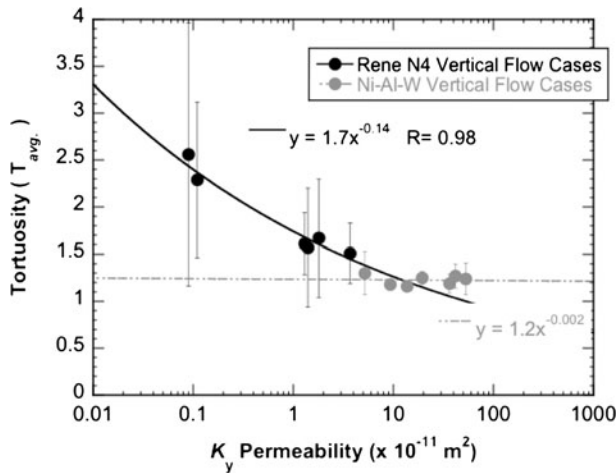


Fig. 8—Tortuosity as a function of permeability for all vertical flow simulation cells in René N4 and Ni-Al-W.

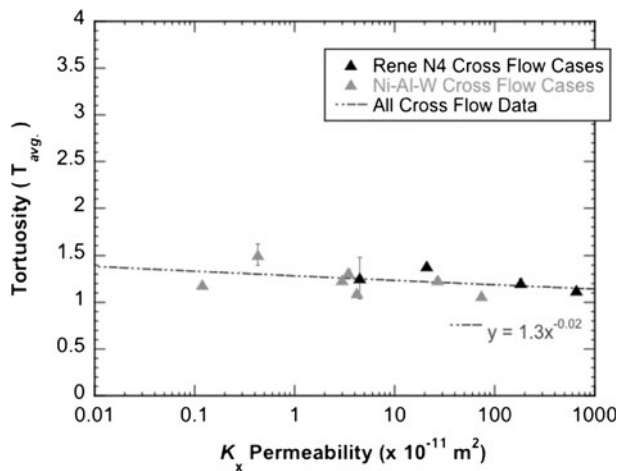


Fig. 9—Tortuosity as a function of permeability for all cross-flow simulation cells in René N4 and Ni-Al-W.

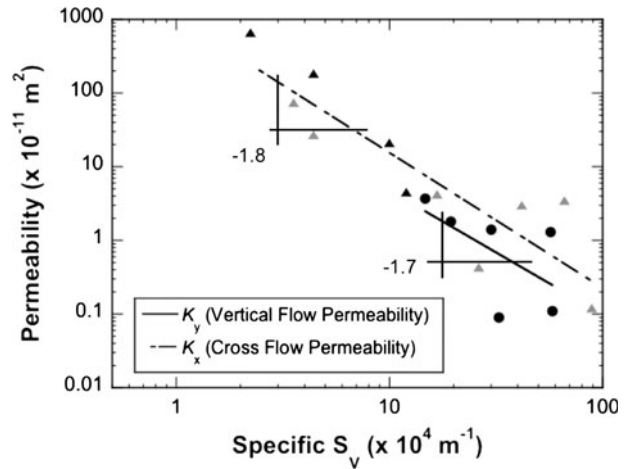


Fig. 10—Permeability as a function of specific S_V in both René N4 and Ni-Al-W simulations.

The variation in permeability with specific S_V across all simulation cells except Ni-Al-W vertical flow cells is shown in Figure 10. An inverse power law dependence of permeability on S_V is observed, *i.e.*, $K = (S_V)^{-n}$. These values of n are only slightly smaller than the dependence of permeability on S_V in the Kozeny-Carmen relation, where $n = 2$ (Eq. [5]). Figure 10 indicates also a tendency toward increases in scatter at high S_V attributable to simulations whose specific S_V is high because contributions of cross-sectional channels did not participate significantly in flow at low liquid fractions.

C. Rayleigh Number Determination

Local Rayleigh numbers (Ra_h) for the René N4 and Ni-Al-W alloy systems were calculated based on the permeabilities obtained in this investigation and compared with Rayleigh values determined by conventional

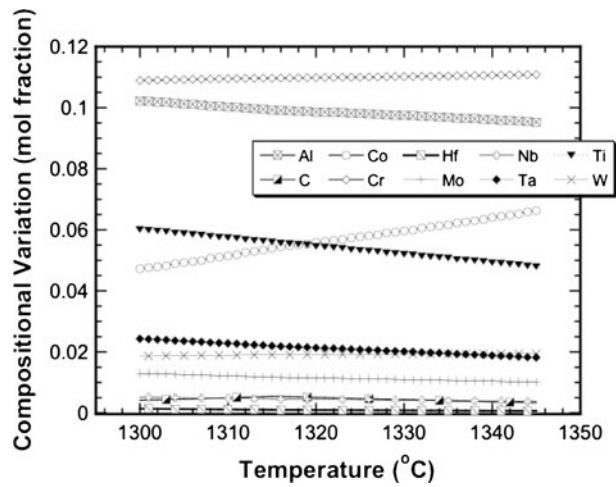


Fig. 11—René N4 compositional variation of alloying elements between liquidus and solidus temperatures determined by PanDat (CompuTherm, LLC).

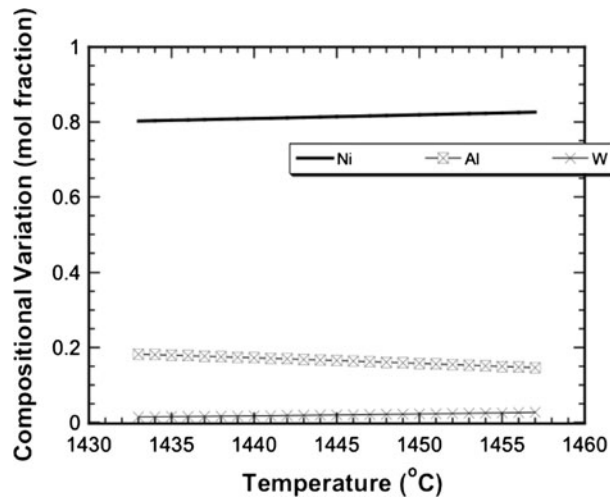


Fig. 12—Ni-Al-W Compositional variation between liquidus and solidus temperatures determined by ThermoCalc.

permeability approximations using Eq. [7]. For all Rayleigh calculations, the product of thermal diffusivity and kinematic viscosity ($\alpha\nu$) were approximated as $5 \times 10^{-12} \text{ m}^4/\text{s}^2$.^[11,15] Determinations of the density gradient were made via an assessment of compositional variation between the liquidus (T_{liquidus}) and solidus (T_{solidus}) temperatures. These variations in both the René N4 and the Ni-Al-W ternary compositions were determined by PanDat, CompuTherm LLC (Pan-Ni database) and ThermoCalc (TCNI:TCS database), respectively and are shown in Figures 11 and 12.

Using these temperature-composition relationships, a solute gradient profile based on the liquidus to solidus temperature difference ($\Delta T_{\text{liquidus-solidus}}$) and experimentally determined thermal gradients were established. This allows for the estimation of temperature-specific densities as a function of the mushy zone height to be computed. Ra_h calculations using these profiles will be denoted as axial ΔT . Alternatively, a height-based

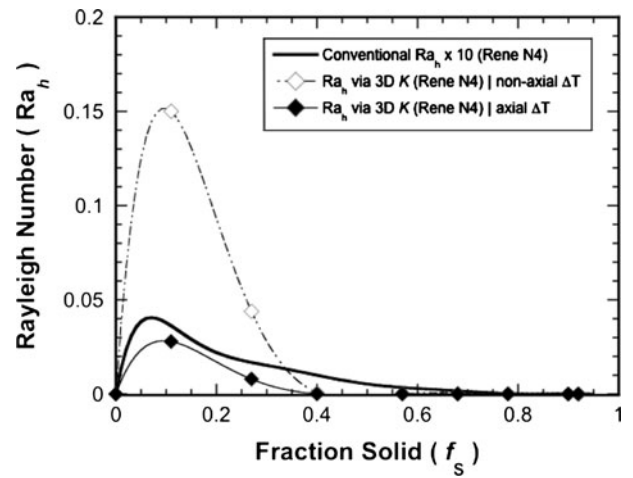


Fig. 13—Local Ra_h for René N4 as a function of solid fraction. Conventional Ra_h is calculated with the permeabilities assessed via Eq. [7]. The remaining Ra_h are calculated with permeabilities from the current study.

thermal profile was determined by fitting the $\Delta T_{\text{liquidus-solidus}}$ difference to the reconstruction heights. Because both reconstruction heights are shorter than predicted by the product of the withdrawal rate and axial thermal gradient present during casting, significant nonaxial heat extraction during casting is a likely explanation for the shortened mushy zone heights. This is probable as samples used in this investigation were extracted from within 1–10 mm of the castings walls. For this reason, the second set of discrete local Ra_h calculations will be denoted as nonaxial ΔT . Both thermal profiles are then used to assess the local compositional variation and the resultant density difference at specific heights allowing for calculation of a local, height-specific Rayleigh number, Ra_h . Both axial ΔT and nonaxial ΔT profiles are combined with the directly assessed 3D dendritic permeabilities for the determination of an axial ΔT Ra_h and a nonaxial ΔT Ra_h prediction. These results are compared with the conventional Ra_h , which has been determined from the permeability approximation of Eq. [7] combined with the CALPHAD-assessed composition variations.

Because both cross and vertical flows are required for convective instabilities to occur, the limiting permeability at each volume fraction is used for the calculation of the local Rayleigh number. In René N4, the lowest permeability occurs for vertical flow at solid fractions above $0.4f_s$, below $0.4f_s$; cross-flow possesses the lower values. In the Ni-Al-W sample, cross flow exhibited the limiting permeability across all volume fractions. In Figures 13 and 14, the conventional Ra_h approximation is compared with axial ΔT Ra_h and nonaxial ΔT Ra_h in René N4 and Ni-Al-W, respectively. While all local Rayleigh calculations show a maximum value in the vicinity of 0.1 fraction solid, 3D-assessed permeabilities yield critical Ra_h values two to three times higher than the conventional approximation. Only the axial ΔT Ra_h in René N4 demonstrates a similar critical value as the conventional Ra_h .

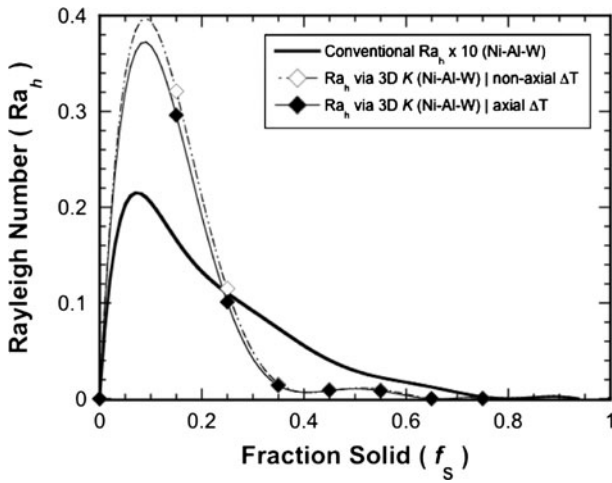


Fig. 14—Local Ra_h for Ni-Al-W as a function of solid fraction. Conventional Ra_h is calculated with permeabilities assessed via Eq. [7], the remaining Ra_h are calculated with permeabilities from the current study.

Overall, the Rayleigh numbers are higher for the Ni-Al-W material, compared with René N4. This finding suggests that convective instabilities will form more easily in the Ni-Al-W material not only because of the solute density inversion, but also because of the higher permeabilities below 0.4 fraction solid. However, because the cross-flow permeability at $f_L = 0.6$ is lower than the vertical permeability in the Ni-Al-W material, the Rayleigh number may not provide an accurate prediction if the flow instabilities originate deep in the mushy zone. Conversely, cross-flow permeabilities across all fraction solid are higher than vertical permeabilities in René N4; therefore, the Rayleigh number should predict convective instabilities rather reasonably.

The analysis herein indicates maximum Rayleigh number in each system are strongly dependent on cross flow permeabilities and occur in the vicinity of 0.1 solid fraction. Additionally, Ra_h curves exhibit a rapid drop after their peak and small values for all fraction solids greater than 0.4. Finally, it should be mentioned that the lower limit in direct permeability assessments of vertical flow in this study also occurs at 0.4 fraction solid because of a lack of contiguous paths of vertical liquid domains over an appreciable length of dendritic structure. However, the analysis based on the Rayleigh number offered in this article indicates that full descriptions of vertical flow at values less than 0.4 fraction solid may not be entirely necessary as critical Ra_h values occur in the vicinity of 0.1–0.2 fraction solid because of cross permeabilities. Furthermore, recent empirical models have suggested cross-flow permeabilities as the limiting flow type^[38,45] in the lower ranges of fraction solid as well.

The calculations reported here also suggest a mechanism for the preferential location of freckles at mold walls and outer boundaries of castings, independent of geometry. The differences in Ra_h affected by variation in thermal profile between axial ΔT and nonaxial ΔT (Figures 13 and 14) illustrate this point. Over the exact

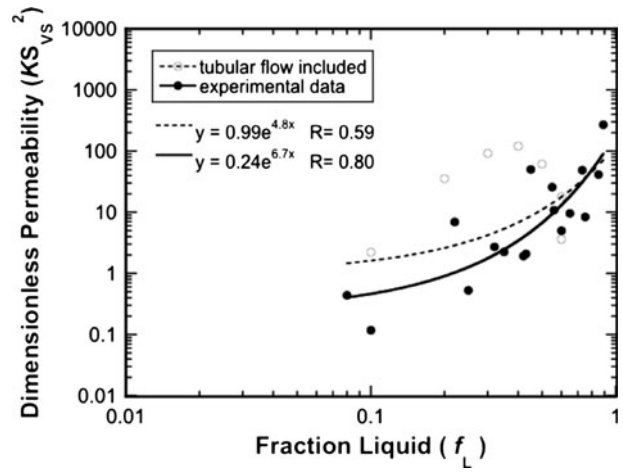


Fig. 15—Dimensionless permeability (KS_{vs}^2) dependence on fraction liquid.

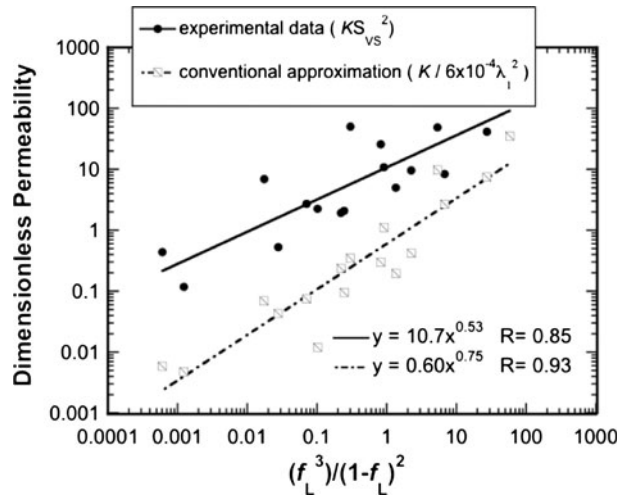


Fig. 16—Experimentally determined dimensionless permeability scaled by the interfacial surface area per unit volume (KS_{vs}^2), the conventional approximation ($K/6 \times 10^{-4} \lambda_1^2$), and the dependence of both on the fraction liquid ratio $(f_L^3)/(1-f_L)^2$.

same dendritic network, significant lateral heat extraction increases the local Rayleigh number dramatically because of a shortening of the mushy zone, forcing the density gradient to occur in a more constrained volume of liquid.

Last, dimensionless permeability across all volume fractions is considered in two ways: first, by scaling K by the interfacial surface area per unit volume solid (S_{vs}), and second, by normalizing by the conventional average permeability, Eq. [7]. In Figure 15, the trend toward maximum dimensionless permeability at high fractions of liquid (*i.e.*, minimum fraction solid) is clear. Furthermore, because S_v is considered implicitly in many permeability models, it is worth considering how currently measured values would influence these models and ultimately how these two aforementioned dimensionless permeabilities compare. Figure 16 illustrates the variation of both dimensionless permeabilities with the quantity $f_L^3/(1-f_L)^2$ present in the Blake-Kozeny

(Eq. [6]) and conventional approximation (Eq. [7]). The empirical fraction liquid ratio derived from Kozeny's seminal work reasonably approximates the increase in permeability in both cases, but here, the experimentally determined permeability is several orders of magnitude higher at any given volume fraction. However, it should be noted that these differences do begin to diminish at very high liquid ratios.

IV. DISCUSSION

It has been demonstrated that direct assessments of permeability based on actual dendritic structure in the mushy zone can be used for improved assessment of permeability and Rayleigh number (Ra_h). In this study, 3D datasets of material at the solid-liquid interface in directionally solidified René N4 and a model Ni-6.5Al-9.5W (wt pct) ternary were used to assess vertical and cross-flow permeabilities directly over the mushy zone. The Rayleigh numbers calculated with experimentally determined permeabilities are higher than those determined with conventional permeability approximations.^[11,14] Additionally, it has been shown that permeability scales inversely with interfacial surface area independent of the degree of flow path tortuosity. As a result, the dimensionless liquid ratio $f_L^3/(1-f_L)^2$ combined with accurate measures of the interfacial surface area can yield more accurate estimates for permeability.

In the systems investigated here, Rayleigh numbers do not exceed a critical value of 1.0 with conventional or 3D dendritic array permeabilities, suggesting instabilities should not occur in either alloy. However, because freckles have been observed in these castings (Figure 1(c)), it is apparent that other physical quantities in the Rayleigh analysis other than permeability, as was focused on here, are not determined adequately. The density gradient ($\Delta\rho/\rho_o$), kinematic viscosity (ν), and the thermal diffusivity (α) are likely sources of error and require additional investigation. With regard to liquid density gradients, there may be errors in the thermodynamic assessments, and currently, insufficient information is available on the liquid density as a function of temperature. Partial molar volume density calculations have been shown to be accurate to within 5 pct^[32,33] for certain alloys; however, a larger error may arise because of uncertainty in the prediction of liquid compositions themselves. The accuracy of phase calculation software is limited by the database used and can vary substantially for unexplored compositions as well as in select commercial nickel-based superalloys with typically three or more elements. Because ($\Delta\rho/\rho_o$) is directly proportional to Ra_h , a variation in density gradient of an order of a magnitude would affect the local Rayleigh number by the same amount. Alternatively, the kinematic viscosity and thermal diffusivity are maintained as constants and are, as a product, considered equal to the value $5 \times 10^{-12} \text{ m}^4/\text{s}^2$.^[11,13,14] Because this consistent approximation is used by various investigators, no discrepancies between the results of this and other investigations are introduced by its use. However,

it is unlikely that kinematic viscosity, thermal diffusivity, or their product remain constant over the entire liquidus to solidus temperature range in most alloys, including those presented in this study. The absence of variation with temperature or composition is likely to have an uncertainty on the order of ± 5 pct for each quantity. Because ($\alpha\nu$) is inversely proportional to Ra_h , a 25 pct increase in the product of the thermal diffusivity and kinematic viscosity would produce a 25 pct decrease in the local Rayleigh number or vice versa. It is, therefore, also reasonable to assert that the greatest amount of error in the current Rayleigh calculations likely reside in either the lack of variation in the quantity ($\alpha\nu$) or the assessment of the actual density gradient across the liquidus to solidus temperature range.

V. CONCLUSIONS

1. Permeability varies inversely with interfacial surface area per unit volume (S_V) for vertical and cross-flow with slightly less sensitivity than the Kozeny-Carmen model.
2. The commercial alloy René N4 has a lower propensity for freckling than the simple Ni-Al-W ternary alloy because of lower permeability in the mushy zone.
3. Tortuosity decreases in vertical flow correlate with increases in permeability up to a value of $10 \times 10^{-11} \text{ m}^2$. In cross flow, tortuosity is largely unchanged at all permeabilities as flow paths in cross flow are largely dictated by the fourfold dendritic symmetry of secondary arms regardless of volume fraction present.
4. Direct permeability assessments show maximum Ra_h values occur in the vicinity of 0.1 fraction solid for the two alloys investigated. Critical Ra_h values are a factor of two to three times higher than conventional Ra_h estimates using the average permeability approximation.
5. Accurate knowledge of interfacial surface area improves permeability prediction in both vertical and cross flow within directionally solidified dendritic structures. When direct assessment is not practical, the following relation reasonably estimates permeability for the alloys considered in this investigation where $C_1 = 10.7$ and $n = 0.5$:

$$K = \frac{C_1}{S_{Vs}^2} \left[\frac{f_L^3}{(1-f_L)^2} \right]^n$$

6. Simulations show higher driving forces for freckle formation are present when significant lateral heat extraction exists during directional solidification. In many cases, this condition exists at or near mold walls, where increases in local Rayleigh number occur as a result. This suggests the mechanism for the appearance of freckles at and along outer walls of castings is related to such lateral heat extraction.

ACKNOWLEDGMENTS

Sandia National Laboratories is a multiprogram laboratory managed and operated by Sandia Corporation, a wholly owned subsidiary of Lockheed Martin Corporation, for the U.S. Department of Energy's National Nuclear Security Administration under contract DE-AC04-94AL85000. The authors are grateful for the technical assistance of C. Torbet, UCSB, as well as support from T. Van Vranken and L. Graham of PCC Airfoils, Inc. The authors have also benefited from useful discussions with C. Beckermann, D. Poirier, P. Voorhees, and J. Dvorkin. The authors also thank C. Woodward, D. Trinkle, and Mark Asta for *ab initio* MD liquidus density calculations. The financial support of the AFOSR MEANS-II Program Grant No. FA9550-05-1-0104 is acknowledged and K. Thornton also acknowledges the support of NSF under Grant No. 0746424.

REFERENCES

1. F.L. Versnyder and M.E. Shank: *Mater. Sci. Eng. A*, 1970, vol. 6 (4), pp. 213–47.
2. F.L. Versnyder and M.E. Shank: *Role of Directional Solidification*, American Society for Metals, Materials Park, OH, 1979, pp. 334–68.
3. R.F. Decker and C.T. Sims: *The Metallurgy of Nickel-Base Alloys*, Wiley, New York, NY, 1972, pp. 97–131.
4. D.N. Duhl: *Single Crystal Superalloys*, Academic Press, San Diego, CA, 1989, pp. 149–82.
5. S.M. Copley, A.F. Giamei, S.M. Johnson, and M.F. Hornbecker: *Metall. Trans.*, 1970, vol. 1, pp. 2193–204.
6. A.F. Giamei and B.H. Kear: *Metall. Trans.*, 1970, vol. 1, pp. 2185–92.
7. T.M. Pollock and W.H. Murphy: *Metall. Mater. Trans. A*, 1996, vol. 27A, pp. 1081–94.
8. G. Muller, G. Neumann, and H. Matz: *J. Crystal Growth*, 1987, vol. 84, pp. 36–49.
9. J.C. Heinrich, S. Felicelli, P. Nandapurkar, and D.R. Poirier: *Metall. Trans. B*, 1989, vol. 20B, pp. 883–91.
10. S. Motakef: *J. Crystal Growth*, 1990, vol. 102, pp. 197–213.
11. C. Beckermann, J.P. Gu, and W.J. Boettinger: *Metall. Mater. Trans. A*, 2000, vol. 31A, pp. 2545–57.
12. W. Yang, K.-M. Chang, W. Chen, S. Mannan, and J. DeBarbadillo: *Metall. Mater. Trans. A*, 2001, vol. 32A, pp. 397–406.
13. J.C. Ramirez and C. Beckermann: *Metall. Mater. Trans. A*, 2003, vol. 34A, pp. 1525–36.
14. S. Tin and T.M. Pollock: *Metall. Mater. Trans. A*, 2003, vol. 34A, pp. 1953–67.
15. S. Tin and T.M. Pollock: *Metall. Mater. Trans. A*, 2004, vol. 39A, pp. 7199–7205.
16. S. Felicelli and D.R. Poirier: *Metall. Mater. Trans. B*, 1998, vol. 29B, pp. 847–55.
17. D. Apelian, M.C. Flemings, and R. Mehrabian: *Metall. Trans.*, 1974, vol. 5B, pp. 2533–37.
18. D. Bernard, O. Nielsen, L. Salvo, and P. Cloetens: *Mater. Sci. Eng. A*, 2005, vol. 392 (1–2), pp. 112–20.
19. M.S. Bhat, D.R. Poirier, and J.C. Heinrich: *Metall. Mater. Trans. B*, 1995, vol. 26B, pp. 1049–56.
20. R. Nasser-Rafi, R. Deshmukh, and D.R. Poirier: *Metall. Trans. A*, 1985, vol. 16A, pp. 2263–71.
21. D.R. Poirier: *Metall. Trans. B*, 1987, vol. 18B, pp. 245–55.
22. R. Mehrabian, M. Keane, and M.C. Flemings: *Metall. Trans.*, 1970, vol. 1B, pp. 1209–20.
23. K. Murakami and T. Okamoto: *Acta Metall.*, 1984, vol. 32 (10), pp. 1741–44.
24. K. Murakami, A. Shiraishi, and T. Okamoto: *Acta Metall.*, 1984, vol. 32 (9), pp. 1423–28.
25. N. Streat and F. Weinberg: *Metall. Trans.*, 1974, vol. 5B, pp. 2539–48.
26. N. Streat and F. Weinberg: *Metall. Trans. B*, 1976, vol. 7B, pp. 417–23.
27. O. Nielsen, L. Arnberg, A. Mo, and H. Thevik: *Metall. Mater. Trans. A*, 1999, vol. 30A, pp. 2455–62.
28. D.R. Poirier and S. Ganesan: *Mater. Sci. Eng. A*, 1992, vol. A157 (1), pp. 113–23.
29. S. Ganesan, C.L. Chan, and D.R. Poirier: *Mater. Sci. Eng. A*, 1992, vol. A151 (1), pp. 97–105.
30. M.S. Bhat, D.R. Poirier, J.C. Heinrich, and D. Nagelhout: *Scripta Met. Mater.*, 1994, vol. 31 (3), pp. 339–44.
31. D. Fuloria, P.D. Lee, and D. Bernard: *Mater. Sci. Eng. A*, 2008, vol. 494 (1–2), pp. 3–9.
32. K. Mukai, Z. Li, and K.C. Mills: *Metall. Mater. Trans. B*, 2005, vol. 36B, pp. 255–62.
33. P.K. Sung, D.R. Poirier, and E. McBride: *Mater. Sci. Eng. A*, 1997, vol. A231 (1), pp. 189–97.
34. J. Spowart: *Scripta Mater.*, 2006, vol. 55, pp. 5–10.
35. J. Madison: Ph.D. Dissertation, The University of Michigan, Ann Arbor, MI, 2010.
36. J. Madison, J. Spowart, D. Rowenhorst, and T.M. Pollock: *JOM*, 2008, vol. 60, pp. 26–30.
37. J. Madison, J. Spowart, D. Rowenhorst, L.K. Aagesen, K. Thornton, and T.M. Pollock: *Acta Mater.*, 2010, vol. 58, pp. 2864–75.
38. J.C. Heinrich and D.R. Poirier: *C.R. Mecanique*, 2004, vol. 332 (5–6), pp. 429–45.
39. P.C. Carmen: *Flow of Gases Through Porous Media*, Academic Press, New York, NY, 1956.
40. G.H. Geiger and D.R. Poirier: *Transport Phenomena In Metallurgy*, Addison-Wesley, Reading, MA, 1973.
41. M.C. Schneider, J.P. Gu, C. Beckermann, W.J. Boettinger, and U.R. Kattner: *Metall. Mater. Trans. A*, 1997, vol. 28A, pp. 1517–31.
42. M.S. Bhat: Ph.D. Dissertation, The University of Arizona, Tucson, AZ, 1995.
43. J. Dvorkin: Private communication, September 27, 2009.
44. G. Mavko, T. Mukerji, and J. Dvorkin: *The Rock Physics Handbook*, Cambridge University Press, Cambridge, UK, 2009.
45. S.M. Roper, S.H. Davies, and P.W. Voorhees: *Metall. Mater. Trans. A*, 2007, vol. 38A, pp. 1069–79.